Bioclimatic traits in statistical properties of daily photosynthetically active radiation

Estefanía Muñoz[1] and Andrés Ochoa[1]

[1]Universidad Nacional de Colombia, Medellín

Correspondence: Estefanía Muñoz (emunozh@unal.edu.co)

Abstract. In this paper, we present a methodology to analyze the stochastic component of daily solar radiation at the earth's surface in the photosynthetically active spectral band. Extraterrestrial solar spectral irradiance from the SOLID project and in situ observed PAR from the FLUXNET data set are used to calculate daily time series of the clearness and clear-sky indices for 28 FLUXNET sites around the world for 1978-2014. We found that the shape of the probability distribution functions of the clearness and clear-sky indices exhibit a spatial pattern related to the Köppen climate classification and the Holdridge life zones. According to the Köppen classification, oceanic, humid continental, and Mediterranean climates show bimodal distributions; semi-arid, temperate, subtropical, and desert climates show unimodal distributions with high dispersion; and tropical climates show unimodal distributions with low dispersion. Moreover, according to the Holdridge triangle, sites with bimodal distributions are concentrated in moist and wet forest life zones located in boreal and cool temperate regions and sub-humid and humid provinces. Unimodal distributions with high dispersion are concentrated in the moist forest life zone in subtropical and tropical regions and humid province; and unimodal distributions with low dispersion are concentrated in dry forest, very dry forest, and thorn woodland in tropical and subtropical regions between arid and subhumid humidity provinces.

1 Introduction

Solar irradiation drives physical, chemical and biological processes at the earth's surface. It is the primary energy source of the natural processes of photosynthesis and evapotranspiration (Bojanowski, 2013; Remesan et al., 2008; Hansen, 1999). The amount of solar irradiance reaching some place on the Earth's surface at a given time is the result of Sun's emission spectrum, Sun–Earth distance, the angle of incidence of solar rays, and the atmospheric attenuation of light. The geometry of Earth's orbit and rotation is well-known and can be calculated with high precision. Attenuation of light throughout the atmosphere can be calculated by using an attenuation law (e.g. the Beer–Lambert law), but this requires to know the atmospheric optical depth, which is seldom the case.

To affront this problem researchers have relied on statistics. Two indices are widely used to quantify the random nature of atmospheric light attenuation, the clear-sky index (c), defined as the ratio of actual radiation to clean-dry atmosphere radiation, and the clearness index (k) which is the ratio of actual radiation to top-of-the-atmosphere radiation (i.e. with no atmospheric attenuation). Although c and k can be calculated for any spectral band and time aggregation scale, they are often studied at the hourly or daily time steps and for the shortwave band.

In this paper, we study the bioclimatic traits on the stochastic behavior of daily c and k for the photosynthetically active radiation (PAR) spectral band. It was possible by using the Solar Spectral Irradiance (SSI) time series, the U.S Standard Atmosphere, and observed PAR time series at 28 FLUXNET sites worldwide, distributed in 13 hexagons of the Holdridge triangle (Holdridge, 1947, 1967) corresponding to 8 life zones.

Table 1. FLUXNET Sites. The record period refers to complete calendar years, i.e. data for all sites start on January 1st of the initial year and end on December 31st of the last year.

Site	Country	Latitude [°]	Longitude [°]	Elevation [m]	Period
AT-Neu	Austria	47.117	11.318	970	2002–2012
BE-Lon	Belgium	50.552	4.746	167	2004–2014
BE-Vie	Belgium	50.305	5.998	493	1996–2014
BR-Sa3	Brazil	-3.018	-54.971	100	2000–2004
CA-Oas	Canada	53.629	-106.198	530	1996–2010
CG-Tch	Congo	-4.289	11.656	82	2006–2009
CH-Oe1	Switzerland	47.286	7.732	450	2002–2008
CH-Oe2	Switzerland	47.286	7.734	452	2004–2014
DE-Geb	Germany	51.100	10.9143	161.5	2001–2014
DE-Gri	Germany	50.950	13.513	385	2004–2014
DE-Hai	Germany	51.079	10.453	430	2000–2012
DE-Obe	Germany	50.787	13.721	734	2009–2014
DE-Tha	Germany	50.962	13.565	385	1996–2014
GF-Guy	French Guiana	5.279	-52.925	48	2004–2014
GH-Ank	Ghana	5.268	-2.694	124	2011–2014
IT-Lav	Italy	45.956	11.281	1353	2003–2014
IT-MBo	Italy	46.015	11.046	1550	2003–2013
IT-SRo	Italy	43.728	10.284	6	1999–2012
MY-PSO	Malaysia	2.973	102.306	148	2003–2009
PA-SPs	Panama	9.314	-79.631	68	2007–2009
RU-Fyo	Russia	56.461	32.922	265	1998–2014
SD-Dem	Sudan	13.283	30.478	500	2005–2009
SN-Dhr	Senegal	15.403	-15.432	40	2010–2013
US-Esm	USA	25.438	-80.595	1.07	2008–2014
US-FPe	USA	48.308	-105.102	634	2000–2008
US-NC2	USA	35.803	-76.668	5	2005–2010
US-SRM	USA	31.821	-110.866	1120	2004–2014
ZA-Kru	South Africa	-25.020	31.497	359	2009–2013

2   Data

Our data set consists of daily observations of incoming photosynthetic photon flux density (PPFD) and rainfall from 28 sites around the world from the FLUXNET data set (Baldocchi et al., 2001; Olson et al., 2004) (Fig. 1). Sites have different periods of record spanning from 1996 to 2014 and elevations from sea level to 1550 m (Table 1). We also use the Solar Spectral

5   Irradiance (SSI) at the top of the atmosphere from the "First European Comprehensive Solar Irradiance Data Exploitation project" (SOLID) (Haberreiter et al., 2017; Schöll et al., 2016) as input data for an atmospheric radiation transfer model (section 3). The SOLID spectral time series has a daily time resolution from 1978/7/11 to 2014/12/31 (13204 days) and covers the wavelength range between 0.5 and 1991.5 nm. Data from SOLID are available at http://projects.pmodwrc.ch/solid.

The wavelength domain for PPFD in the FLUXNET data set is 400–700 nm (Olson et al., 2004) and has units of $\mu mol\ m^{-2}\ s^{-1}$.

10   We convert PPFD to PAR irradiance in $W\ m^{-2}$ through the relationship 4570 nmol m^{-2} s^{-1}=1 W m^{-2} (Sager and McFarlane, 1997).

Information of Köppen climate classification and Holdridge life zones is taken from Rubel and Kottek (2010) and NEP-WCMC, respectively.
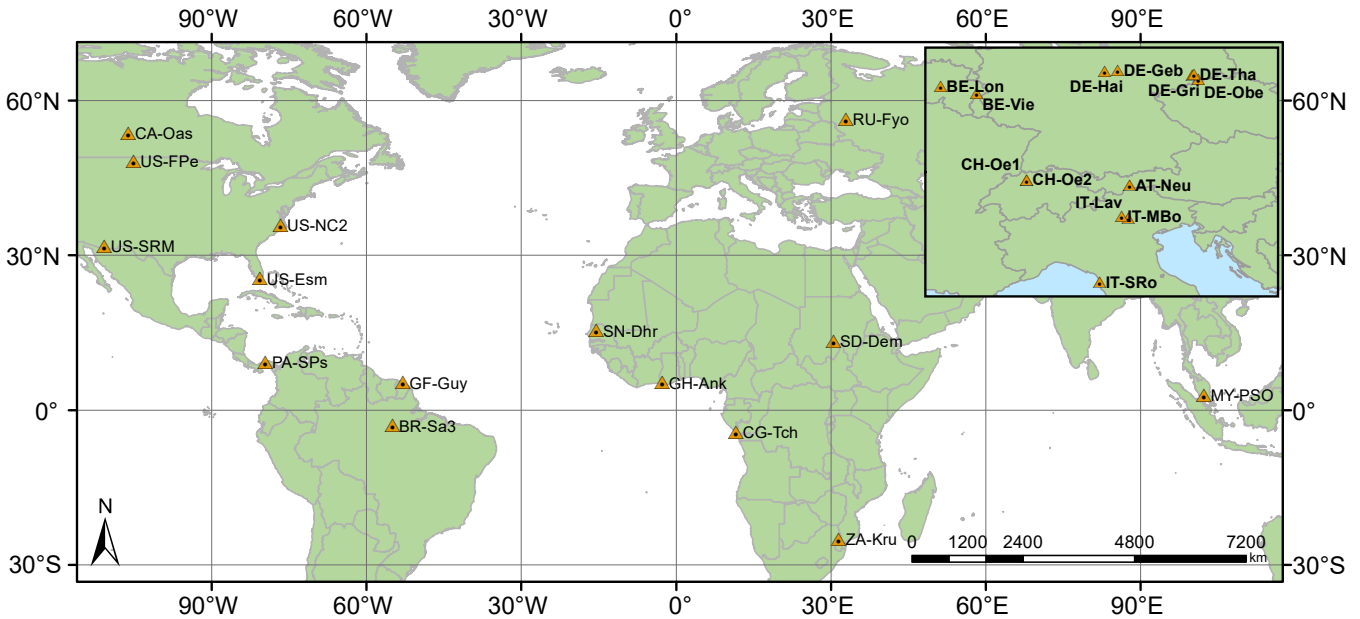
Figure 1. The sites selected from the FLUXNET dataset are spanned over several continents and climates.

3 Methods

Daily radiation amount at a site on the earth's surface is the result of integrating instantaneous irradiance over the day length. Surface instantaneous irradiance estimation comprises solar irradiance at the top of the atmosphere (TOA) and the physical properties of the atmosphere for the site and time of interest. We use SOLID data for TOA irradiance and the Beer–Lambert law

5 to calculate light attenuation by the atmosphere. However, some atmospheric components as clouds, water vapor, and aerosols are highly variable in space and time, which is troublesome when using the Beer–Lambert law. Therefore, we follow two approaches: 1) use the clear-day index (c) (also known as relative clearness index, clear day index, and normalized clearness index) to assess the effect of the variable components on total daily radiation, and 2) use the clearness index (k) to assess the whole atmospheric effect on total daily radiation. Both indices are defined in Eqs. (1), where PAR_{obs} is the observed daily

10 global PAR on a horizontal surface at the ground level, PAR_0 is the extraterrestrial daily global PAR on a horizontal surface, and PAR_{cda} is the daily global PAR on a horizontal surface on the ground for a cloudless, clean, and dry atmosphere.

$$c = \frac{PAR_{obs}}{PAR_{cda}}, \quad k = \frac{PAR_{obs}}{PAR_0} \tag{1}$$

3.1 PAR at the top of the atmosphere

Photosynthetically active radiation at the top of the atmosphere (PAR_0) is calculated by integrating the daily SSI over the PAR

15 spectral band (400–700 nm) to obtain the Total Spectral Irradiance (TSI_{PAR}), as shown in Eq. (2) and doing the geometric

transformations accounting for solar declination (δ) and latitude (ϕ), as shown in Eq. (3) (Iqbal, 1983).

$$TSI_{PAR} = \int\limits_{400\ nm}^{700\ nm} SSI\,\mathrm{d}\lambda \tag{2}$$

$$PAR_0 = \frac{24E_0}{\pi} TSI_{PAR} \left(\omega_{sr} \sin\delta \sin\phi + \cos\delta \cos\phi \sin\omega_{sr} \right) \tag{3}$$

where E_0 is the eccentricity correction factor of the earth's orbit and ω_{sr} is the sunrise hour angle for the day.

5 ## 3.2 Surface PAR for a cloudless, clean dry atmosphere

Surface PAR for a cloudless, clean, and dry atmosphere (PAR_{cda}) is the sum of the direct (PAR_b) and diffuse (PAR_d) components ($PAR_{cda} = PAR_b + PAR_d$). To calculate daily PAR_b and PAR_d on a horizontal surface at the ground level, we model the direct and diffuse instantaneous spectral irradiances and integrate them along the day length and the PAR spectral domain.

10 Following Iqbal (1983), we assume the cloudless, clean and, dry atmosphere to be composed by uniformly mixed gases (m) and ozone (o). Using the Beer–Lambert law and integrating, daily PAR_b is calculated as in Eq. (4).

$$PAR_b = \int\limits_{\gamma_{sr}}^{\gamma_{ss}} \int\limits_{400\ nm}^{700\ nm} SSI_{0,n,\lambda} E_0 \sin(\gamma) \tau_{ma,\lambda}\,\mathrm{d}\lambda\,\mathrm{d}\gamma \tag{4}$$

where $SSI_{0,n,\lambda}$ is the extraterrestrial spectral irradiance normal to the rays from the sun (obtained from SOLID), γ is the solar altitude varying from sunrise (sr) to sunset (ss), and $\tau_{ma,\lambda}$ is the transmittance due to molecular absorbers of the atmosphere.

15 For the assumed atmosphere composition $\tau_{ma,\lambda} = \tau_o \cdot \tau_g$, where τ_o and τ_g are the ozone and the mixed gases transmittance, respectively (see details in Iqbal, 1983, Sec.6.14). Assuming forward and backward scatterances of 0.5 and considering only the first pass of radiation through the atmosphere, PAR_d can be calculated by

$$PAR_d = \int\limits_{\gamma_{sr}}^{\gamma_{ss}} \int\limits_{400\ nm}^{700\ nm} SSI_{0,n,\lambda} E_0 \sin(\gamma) \tau_{ma,\lambda} [0.5(1 - \tau_{r,\lambda})]\,\mathrm{d}\lambda\,\mathrm{d}\gamma \tag{5}$$

20 where $\tau_{r,\lambda}$ is the transmittance due to Rayleigh molecular scattering (see details in Iqbal, 1983, Sec.6.14).

Several atmospheric parameters are required by Eqs. (4) and (5). We assume the 1976 U.S. standard atmosphere (NASA, 1976) (sea level pressure of 101.325 kPa, sea level temperature of 288 K, and sea level density of 1.225 kg/m^3) and the Kasten and Young (1989, Table II) optical air mass function of solar altitude, which has 336 values for solar altitudes between 0° and 90°. Transmittance for ozone and mixed gases are calculated as in Eqs. (6) to (8).

25 $\tau_{o,\lambda} = \exp(-k_{o,\lambda} l_o m_r)$ \hfill (6)

$$\tau_{g,\lambda} = \exp\left[\frac{-1.41 k_{g\lambda} m_a}{(1 + 118.93 k_{g\lambda} m_a)^{0.45}}\right] \tag{7}$$

$$\tau_{r,\lambda} = \exp(0.008735 \lambda^{-4.08} m_a) \tag{8}$$

5 where m_r is relative air mass at standard pressure, m_a is relative air mass at actual pressure, k_o and k_g are the absorption attenuation coefficient for oxygen and mixed gases, and l_o is the amount of ozone in cm (at normal temperature and pressure, NTP). We calculate $k_{o,\lambda}$ for any λ value using the Leckner (1978) interpolation of the classic Vigroux (1953) data. For calculating l_o we interpolate Table 5.3.2 from Iqbal (1983), which is a reproduction of Robinson (1966, p.114). $k_{o,\lambda}$ is calculated by interpolating Table 6.13.1, which is a reproduction of Table 4 in Leckner (1978, p.146).

3.3 Statistical properties of k and c

We estimate the daily time series, annual cycles, autocorrelograms, and empirical probability density functions (PDF) of c and k. We separate the data of c and k by rainy and dry days, using precipitation as a proxy of cloudiness and water vapor in the atmosphere. Then, we inspect the seasonality of c and k by comparing the cumulative distribution function (CDF) of each month with the CDFs of the other months. The comparison of the CDFs is carried out visually and tested by using Kolmogorov–Smirnov (KS) and Anderson–Darling (AD) Goodness of Fit Tests (Dodge, 2008; Pearson, 1900; Scholz and Stephens, 1987).

4 Results and Discussion

The time series, annual cycle, and autocorrelogram of PAR, c and k were calculated and plotted for each site. The results for AT-NEU are shown in Fig. 2, and those for all other sites are in Figs. S1 to S28. Notice that some values of c and k are greater than 1 during winter in sites with seasonal snow. This anomaly can be explained by the multiple reflection of light enhanced by the snow cover.

The autocorrelograms of PAR, c, and k indicate a more marked annual cycle for PAR than for c and k (see Fig. 2), except at most of the tropical sites (BR-Sa3, CG-Tch, GF-Guy, GH-Ank, MY-PSO, PA-SPs, SD-Dem, and ZA-Kru). All tropical sites have a very weak autocorrelation function (ACF), while extratropical sites show strong ACFs of PAR. Clearness and clear-sky indices remove the astronomical seasonality, indicating that PAR seasonality in extratropical sites is almost entirely explained by the astronomical seasonality. The above is pointed out by the weaker ACFs of k and c when compared with the ACF of PAR. In these sites, climatic seasonality is very weak since the low ACF after removing the astronomical seasonality. In contrast, tropical sites show a seasonality almost completely explained by the climatic seasonality (and not by the astronomical seasonality), being the ACF of the indices and PAR very similar.
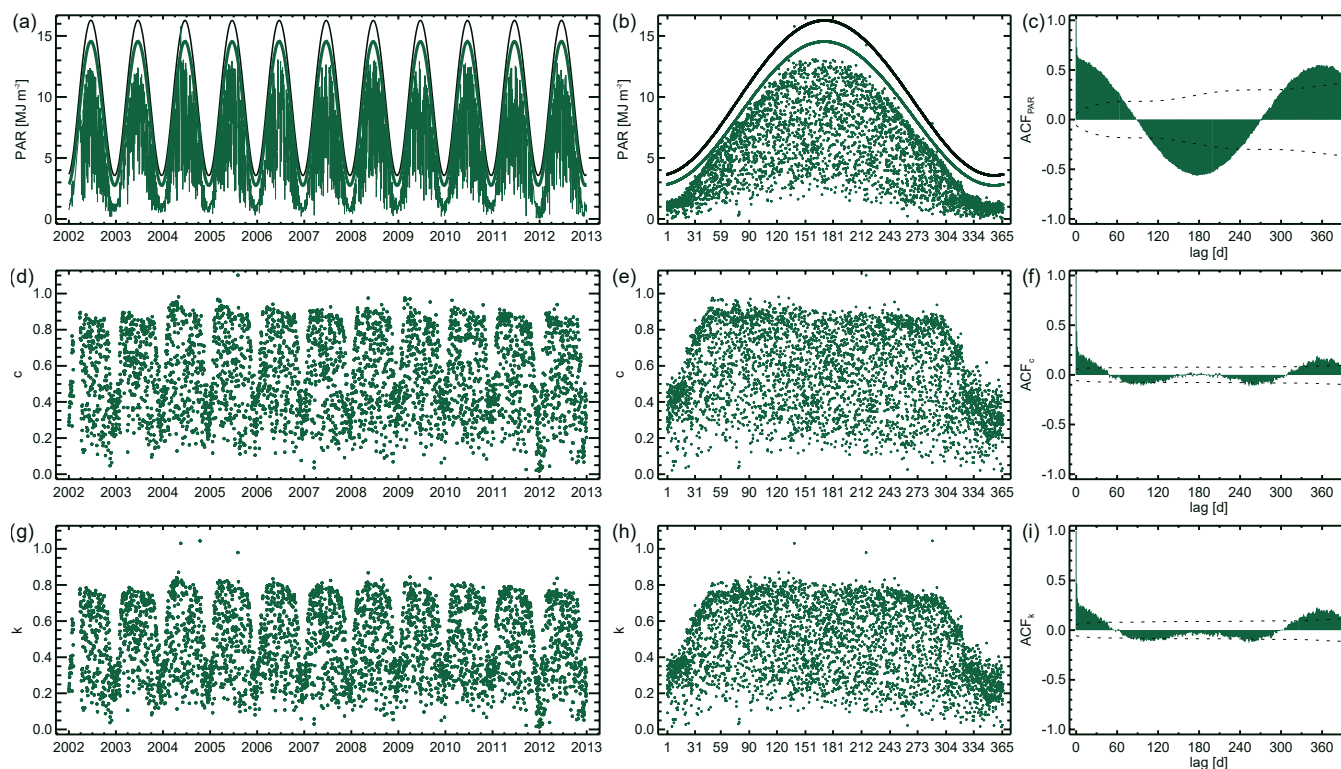
Figure 2. Time series, annual cycle, and autocorrelation function of PAR (a–c), c (d–f), and k (g–i) at AT-Neu.

The ACF of k is stronger than that of c in most sites (Fig. 2, panels f and i). The calculation of k does not include any atmosphere, while c considers a cloudiness-sky, clean, and dry atmosphere. The high ACFs of k suggest that the atmosphere (specifically the air mass) has seasonality, that k does not manage to remove (Ianetz and Kudish, 2008).

ACFs show a period of 180 days approximately for all the sites studied, except in BR-Sa3 where it is 120 days (for both PAR
5   and the indices), and in AT-Neu where it is 80 days (only for the indices). As seasonality depends largely on the movement of the sun, the periods in sites nearest to the geographical Equator should be shorter than those of extratropics, as in BR-Sa3. However, seasonality is also a function of local factors not dealt with in this paper. The differences in the periods of PAR and its indices in AT-Neu can be explained because the climatic and astronomical seasonalities are out of phase.

The pdfs of c and k reveal a certain degree of bimodality, or at least, some asymmetry in respect to the mean, as mentioned
10 before by Hollands and Suehrcke (2013); Tovar-Pescador (2008); Assunção et al. (2003); Ibánez et al. (2003); Jurado et al. (1995); Skartveit and Olseth (1992); Olseth and Skartveit (1984) (see Fig. S29 to S56). We classified the pdfs of c and k in three types: Bimodal, Unimodal I (unimodal with low dispersion), and Unimodal II (unimodal with high dispersion). Sites in the extratropical northern hemisphere (except the site in the United States US-Fep) have bimodal distributions; sites in tropics, subtropics, and US-Fpe have Unimodal II distributions; and sites in tropics have Unimodal II distributions. The same behavior

is observed for k and c. This led us to suspect that k and c follow bimodal distributions in high latitudes, unimodal distributions with high dispersion in mid-latitudes, and unimodal distributions with low latitudes.

Looking for spatial patterns in the PDF shapes of daily c and k, we arranged sites following the Köppen classification and Holdridge life zones (Holdridge, 1947, 1967). According to the Köppen classification, bimodality occurs in oceanic, humid

5 continental, and Mediterranean climates; unimodal PDFs with high dispersion in tropical monsoon, tropical savanna, and tropical rainforest climates; and unimodal PDFs with low dispersion in semi-arid, temperate, subtropical humid, and desert climates.

The Holdridge life zones triangle has the advantage of allowing to analyze schematically the link between climate and long-term behavior of c and k. Red symbols in Fig. 3 represent the sites with bimodal PDFs of k and c, purple symbols the sites with

10 unimodal I PDFs, and yellow symbols the sites with unimodal II PDFs. Bimodality is concentrated in moist and wet forest life zones in the cool temperate and boreal regions on subhumid and humid provinces. Sites in moist and wet forest life zones in humid tropical and subtropical regions on the humid province have Unimodal II distributions, and sites dry forest, very dry forest, and thorn woodland life zones have Unimodal I distributions. The latter are in the tropical and subtropical regions on humidity provinces between arid and subhumid. Although US-Fpe has Unimodal I PDF and is located in the cool temperate

15 region, it stays in the same range of humidity provinces as the other sites with this type of PDF (i.e., arid to subhumid). Fig. 3 allows us to infer the high influence of latitude and the type of climate on the statistical behavior of c and k.

Fig. 4 shows the PDFs (left panel) and the CDFs (right panel) for wet (blue) and dry (red) days of c (a–b) and k (c–d). Figs. 26 to 56 show the results of the 28 sites analyzed. Because bimodality is attributed to clear and overcast sky conditions (Tovar-Pescador, 2008; Olseth and Skartveit, 1984), by separating the values of c and k on rainy and dry days, bimodal PDFs

20 are divided into two unimodal ones, except for AT-Neu, DE-Geb, and DE-Hai, where the PDFs of dry days continue to have a bimodal distribution. This can be explained by the presence and absence of clouds on dry days since there is not always a direct relationship between rainfall and clouds.

After separating data by rainy and dry days, we divided them by months to define the seasons of the indices. Fig. 5 shows the CDF of each month separated by rainy (blue lines) and dry (red lines) days (a–b), and the comparison matrices of the PDF

25 of each month (c–j) at the AT-Neu site. Values into cells are the p-values obtained with KS and AD Goodness of Fit Tests. Figs. S57 to S84 show the results of all sites studied. The definition of index seasons is very clear in the extratropical sites since the CDFs of months with low values of c and k are notoriously thrown to the left side, and the months with high values to the right side, both for rainy and dry days (see Fig. 5(a–b)). Besides, the matrices of comparison corroborate it. Nevertheless, at sites within or near the tropics, the monthly CDFs are not markedly grouped, and matrices of comparison do not indicate clear

30 seasons.

At most sites, it is possible to define two seasons: Season 1 (Season 2) includes the period in which high (low) values of k and c are more likely. In the extratropical northern hemisphere, Season 1 (Season 2) occurs approximately between November (March) and February (September). We notice that at many sites there is a transition between seasons, but it is not considered here. Furthermore, at most tropical sites, there is no precise differentiation of seasons.

Figure 3. Holdridge's life zones triangle. The 28 FLUXNET sites of this study are distributed in 13 hexagons corresponding to 8 life zones.
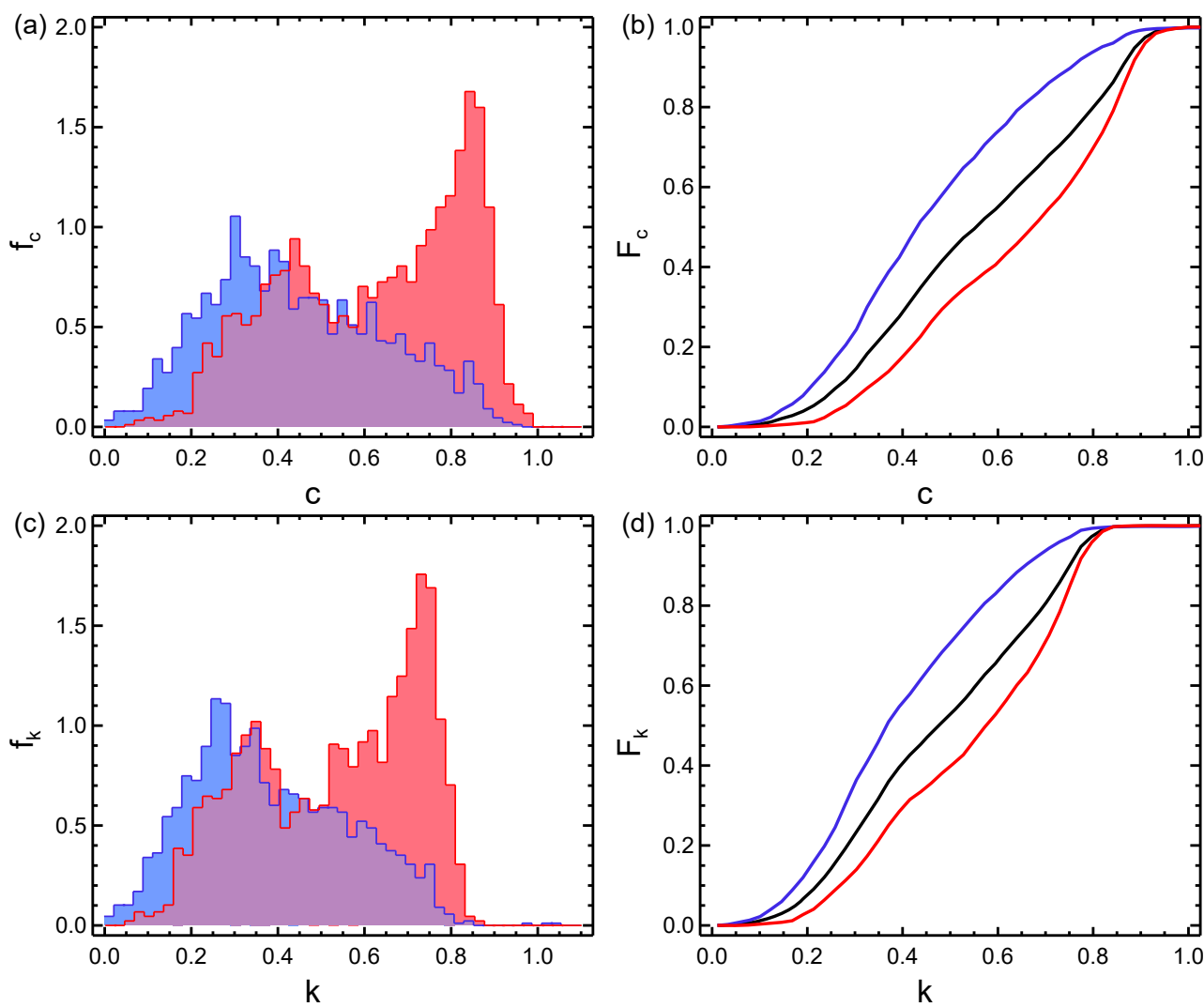
Figure 4. PDFs and CDFs for wet (blue) and dry (red) days of (a–b) c and (c–d) k at AT-Neu FLUXNET site.
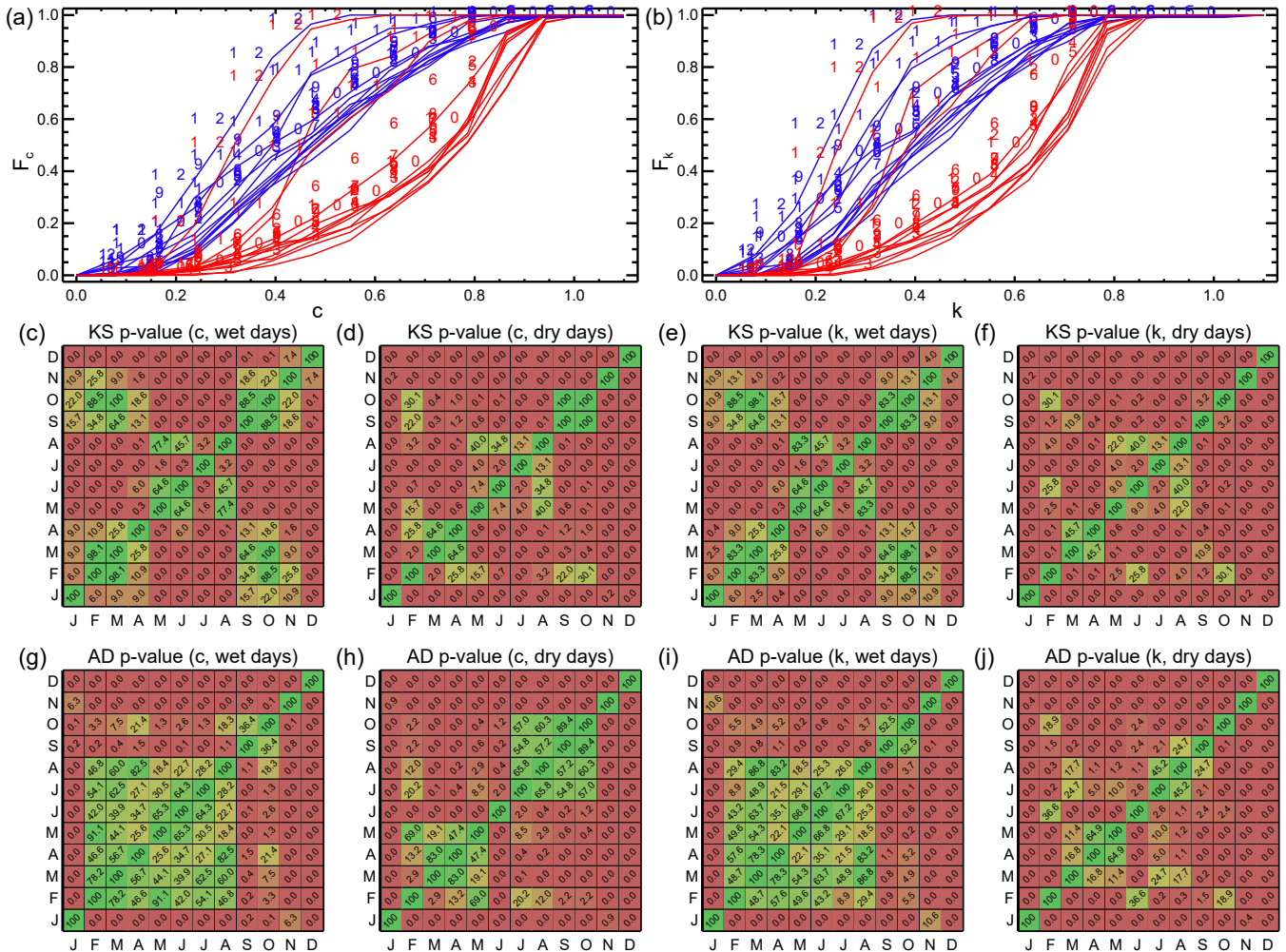
Figure 5. Monthly CDFs of (a) c, and (b) k. (c–j) p-value of the 2-sample KS and AD tests applied to all combinations of monthly CDF of c and k during wet (blue) and dry (red) days at AT-Neu.

The beginning and the end of seasons do not change notably with the index (k and c), but they do with the occurrence or non-occurrence of rainfall. Only at IT-MBo, US-Esm and US-NC2, they do not change. At the other sites, season 1 is usually shorter than season 2 for dry days, and longer than season 2 for rainy days. When analyzing the changes in the beginning and the end of the seasons according to the Holdridge life zones, we do not observe clear patterns. This may indicate that local factors control when the seasons of the indices begin and end.

Fig. 6 shows the relationship between the clearness and the clear-sky indices. The graphics are sorted in descending order of latitude, and each color dot indicates a month. Black dots represent the days in January, green dots the days in July, and red dots the days in December. From Eqs. (1), the slope of lines (m) is given by PAR_0/PAR_{cda}. As PAR_0 does not consider the absorption by atmosphere components, it has a higher value than PAR_{cda} that does it, being m always greater than 1. Sites in
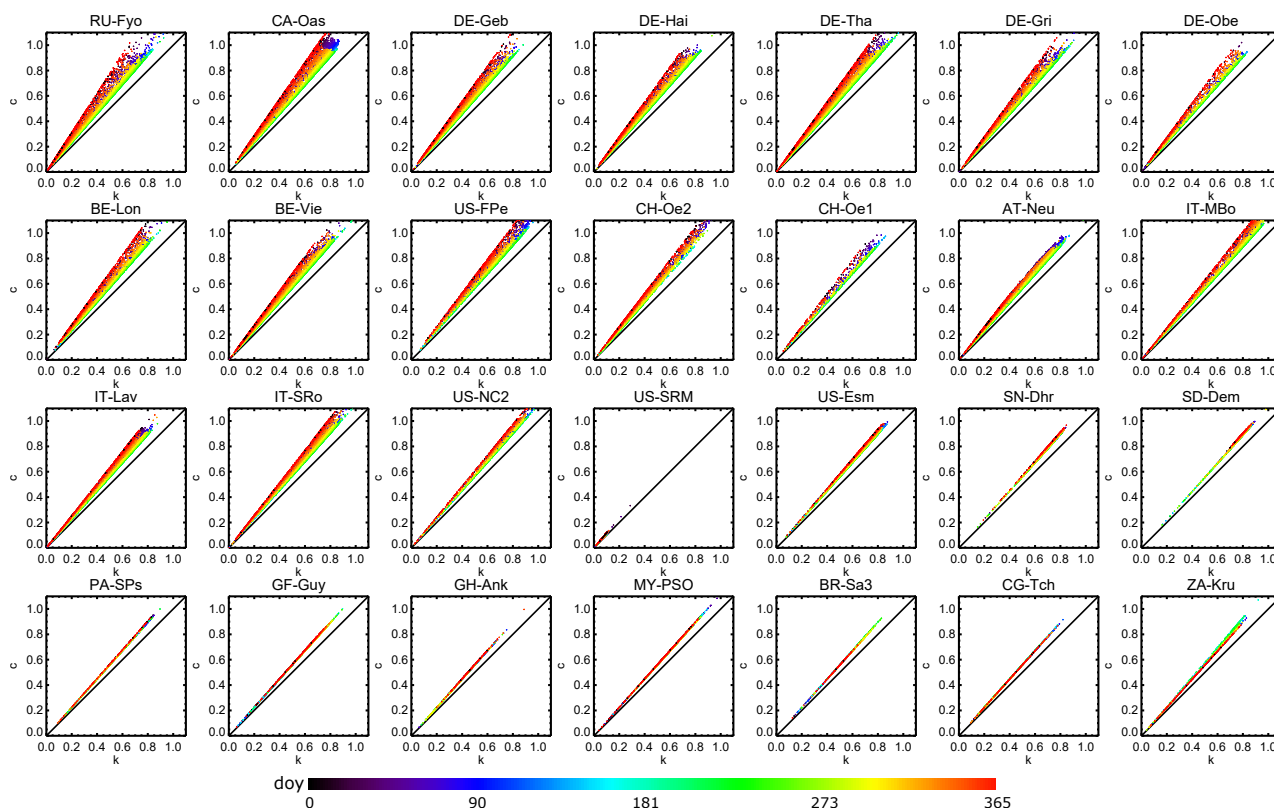
Figure 6. Relationship between k and c. Graphs are sorted by decreasing latitude from the top-left to the bottom right. Colors indicate the day of the year (doy)

high northern latitudes show a notable variability of m throughout the year, while in the tropics and the southern hemisphere, the dispersion is very low.

Fig. 7 shows the daily eccentricity correction factor (E_0) (orange line) and the relative air mass (purple lines) for different latitudes. E_0 denotes the Sun–Earth distance for any day of the year, indicating the potential energy arriving at the Earth's

5 surface when there is no atmosphere. In the extratropical latitudes, m_a has a great variation, while in the tropics it is almost constant (dotted line). The changes in m_a explain the high dispersion of m in high latitudes and the low dispersion at sites near the equator. In northern high latitudes, the largest differences between c and k occur at the beginning and the end of the year since the path length that light rays must pass through is longer than in the middle of the year.

We analyzed the stochastic behavior of the daily clearness and clear-sky indices for the photosynthetically active spectral

10 domain. Both indices remove the astronomical seasonality, and c also removes the seasonality of the clean and dry air optical mass. Therefore, c is neater than k in describing the effect of the highly variable components of the atmosphere, i.e., clouds, water vapor, and aerosols.
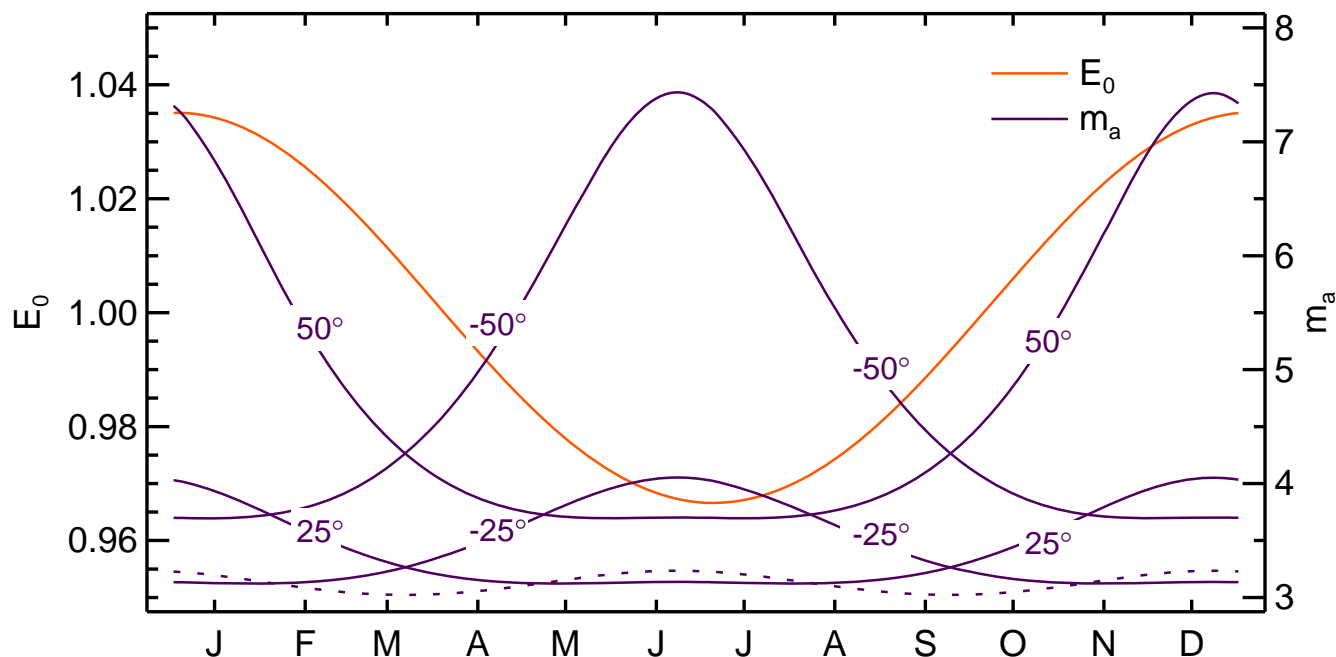
Figure 7. Daily variability of eccentricity correction factor and optical mass for several latitudes.

Due to the multiple refractions of light by snow, we found values of c and k greater than 1 in sites where there is seasonal snow, during the periods in which it occurs.

The analysis of rainy and dry days revealed that c and k have similar statistical shape PDFs as indicated by Escobedo et al. (2009), but k exposed higher values than c. The differences between c and k are more accentuated in the extratropical northern hemisphere since the path length that energy must pass through varies considerably during the year. Besides, in the extratropical northern hemisphere, c shows lower autocorrelations than k for all the lags analyzed, indicating that the air mass of the atmosphere has seasonality, and k does not manage to remove it.

By locating the 28 sites analyzed on the Holdridge life zones scheme (see Fig. 3), we noticed that the geographical location and climate greatly influence the statistical behavior of c and k. High latitudes sites exhibit bimodal distributions, arid to sub-humid climates exhibit unimodal distributions with high dispersion, and humid tropical regions exhibit unimodal distributions with low dispersion.

As rainfall is a proxy of cloudiness and water vapor, bimodal distributions vanish when data are divided into rainy and dry days, corroborating that each mode is related to clear and overcast skies conditions (Tovar-Pescador, 2008; Olseth and Skartveit, 1984).

On the seasonality, we found a clear definition of indices seasons at extratropical sites, unlike tropical sites where local conditions play a determining role. Variations in the beginning and end of indices seasons do not show a notorious spatial

pattern. In fact, it is possible to see different behaviors in a similar geographical location, as at the two sites in Belgium. This also can be attributed to local conditions.

The results obtained in this analysis are useful in a large number of study areas, such as those related to ecohydrology, meteorology, glaciology, agroclimatology, etc. Furthermore, this methodology can be extended to any site and any radiation

5 wavelengths range between 0.5 and 1991.5 nm.

Author contributions. EM and AO conceived the idea. AO calculated the clear-sky daily radiation. EM calculated all the statistics. Both EM and AO analyzed the results and wrote the manuscript. AO supervised the work.

Acknowledgements. We thank Departamento Administrativo de Ciencia, Tecnología e Investigación de Colombia (Colciencias) and Universidad Nacional de Colombia for financial support through the "Becas de Doctorado Nacionales" program, and the "Convocatoria para el

10 Apoyo al Desarrollo de Tesis de Posgrado de la Universidad Nacional de Colombia 2018", respectively. This work used data acquired and shared by the FLUXNET community and the SOLID Project.

References

Assunção, H. F., Escobedo, J. F., and Oliveira, A. P.: Modelling frequency distributions of 5 minute-averaged solar radiation indexes using Beta probability functions, Theoretical and Applied Climatology, 75, 213–224, https://doi.org/10.1007/s00704-003-0733-9, 2003.

Baldocchi, D., Falge, E., Gu, L., Olson, R., Hollinger, D., Running, S., Anthoni, P., Bernhofer, C., Davis, K., Evans, R., Fuentes, J., Goldstein, A., Katul, G., Law, B., Lee, X., Malhi, Y., Meyers, T., Munger, W., Oechel, W., Paw, K. T., Pilegaard, K., Schmid, H. P., Valentini, R., Verma, S., Vesala, T., Wilson, K., and Wofsy, S.: FLUXNET: A New Tool to Study the Temporal and Spatial Variability of Ecosystem–Scale Carbon Dioxide, Water Vapor, and Energy Flux Densities, Bulletin of the American Meteorological Society, 82, 2415–2434, https://doi.org/10.1175/1520-0477(2001)082<2415:FANTTS>2.3.CO;2, 2001.

Bojanowski, J.: Quantifying Solar Radiation At the Earth Surface With Meteorological and Satellite Data, Phd, University of Twente, 2013.

Dodge, Y.: The Concise Encyclopedia of Statistics, Springer New York, New York, NY, https://doi.org/10.1007/978-0-387-32833-1, 2008.

Escobedo, J. F., Gomes, E. N., Oliveira, A. P., and Soares, J.: Modeling hourly and daily fractions of UV, PAR and NIR to global solar radiation under various sky conditions at Botucatu, Brazil, Applied Energy, 86, 299–309, https://doi.org/10.1016/j.apenergy.2008.04.013, 2009.

Haberreiter, M., Schöll, M., Dudok de Wit, T., Kretzschmar, M., Misios, S., Tourpali, K., and Schmutz, W.: A new observational solar irradiance composite, Journal of Geophysical Research: Space Physics, 122, 5910–5930, https://doi.org/10.1002/2016JA023492, 2017.

Hansen, J. W.: Stochastic daily solar irradiance for biological modeling applications, Agricultural and Forest Meteorology, 94, 53–63, https://doi.org/10.1016/S0168-1923(99)00003-9, 1999.

Holdridge, L. R.: Determination of World Plant Formations From Simple Climatic Data, Science, 105, 367–368, https://doi.org/10.1126/science.105.2727.367, 1947.

Holdridge, L. R.: Life zone ecology, Tropical Science Center, San Jose, Costa Rica, 1967.

Hollands, K. G. T. and Suehrcke, H.: A three-state model for the probability distribution of instantaneous solar radiation, with applications, Solar Energy, 96, 103–112, https://doi.org/10.1016/j.solener.2013.07.007, 2013.

Ianetz, A. and Kudish, A.: A method for determining the solar global and defining the diffuse and beam irradiation on a clear day, in: Modeling Solar Radiation at the Earth's Surface: Recent Advances, edited by Badescu, V., chap. 4, pp. 93–113, Springer-Verlag Berlin Heidelberg, https://doi.org/10.1007/978-3-540-77455-6_4, 2008.

Ibánez, M., Rosell, J. I., and Beckman, W. A.: A bi-variable probability density function for the daily clearness index, Solar Energy, 75, 73–80, 2003.

Iqbal, M.: An Introduction to Solar Radiation, Academic Press, Toronto, 1983.

Jurado, M., Caridad, J. M., and Ruiz, V.: Statistical distribution of the clearness index with radiation data integrated over five minute intervals, Solar energy, 55, 469–473, https://doi.org/10.1016/0038-092X(95)00067-2, 1995.

Kasten, F. and Young, A. T.: Revised optical air mass tables and approximation formula, Applied Optics, 28, 4735, https://doi.org/10.1364/AO.28.004735, 1989.

Leckner, B.: The spectral distribution of solar radiation at the earth's surface—elements of a model, Solar Energy, 20, 143–150, https://doi.org/10.1016/0038-092X(78)90187-1, 1978.

NASA: U.S. Standard Atmosphere, 1976, Tech. rep., NOAA, Washington, D.C., 1976.

Olseth, J. A. and Skartveit, A.: A probability density function for daily insolation within the temperate storm belts, Solar Energy, 33, 533–542, https://doi.org/10.1016/0038-092X(84)90008-2, 1984.

Olson, R., Holladay, S., Cook, R., Falge, E., Baldocchi, D., and Gu, L.: FLUXNET. Database of fluxes, site characteristics, and flux-community information, Tech. rep., Oak Ridge National Laboratory (ORNL), Oak Ridge, TN (United States), https://doi.org/10.2172/1184413, 2004.

Pearson, K.: X. On the criterion that a given system of deviations from the probable in the case of a correlated system of variables is such

5   that it can be reasonably supposed to have arisen from random sampling, The London, Edinburgh, and Dublin Philosophical Magazine and Journal of Science, 50, 157–175, https://doi.org/10.1080/14786440009463897, 1900.

Remesan, R., Shamim, M. A., and Han, D.: Model data selection using gamma test for daily solar radiation estimation, Hydrological Processes, 22, 4301–4309, https://doi.org/10.1002/hyp.7044, 2008.

Robinson, N.: Solar Radiation, Elsevier, Amsterdam, 1966.

10   Rubel, F. and Kottek, M.: Observed and projected climate shifts 1901-2100 depicted by world maps of the Köppen-Geiger climate classification, Meteorologische Zeitschrift, 19, 135–141, https://doi.org/10.1127/0941-2948/2010/0430, 2010.

Sager, J. C. and McFarlane, J. C.: Radiation, in: Growth Chamber Handbook, edited by Langhans, R. and Tibbitts, T., pp. 1–30, NC-101 Committee on Controlled Environment Technology and Use, 1997.

Schöll, M., Dudok de Wit, T., Kretzschmar, M., and Haberreiter, M.: Making of a solar spectral irradiance dataset I: observations, uncertain-

15   ties, and methods, Journal of Space Weather and Space Climate, 6, https://doi.org/10.1051/swsc/2016007, 2016.

Scholz, F. and Stephens, M.: K-Sample Anderson-Darling Tests, Journal of the Amerlcan Statistical Association, 82, 918–924, https://doi.org/10.2307/2288805, 1987.

Skartveit, A. and Olseth, J. A.: The probability density and autocorrelation of short-term global and beam irradiance, Solar Energy, 49, 477–487, https://doi.org/10.1016/0038-092X(92)90155-4, 1992.

20   Tovar-Pescador, J.: Modelling the statistical properties of solar radiation and proposal of a technique based on Boltzmann statistics, in: Modeling Solar Radiation at the Earth's Surface: Recent Advances, edited by Badescu, V., chap. 3, pp. 55–91, Springer-Verlag Berlin Heidelberg, https://doi.org/10.1007/978-3-540-77455-6_3, 2008.

Vigroux, E.: Contribution à l'étude expérimentale de l'absorption de l'ozone, Annales de Physique, 12, 709–762, https://doi.org/10.1051/anphys/195312080709, 1953.